Spatiotemporal modeling of direct acceleration with high-field terahertz pulses

ZOLTÁN TIBAI,[1,5] SZABOLCS TURNÁR,[1] GYÖRGY TÓTH,[1] JÁNOS HEBLING,[1,2,3] AND SPENCER W. JOLLY[4,6]

[1]*Institute of Physics, University of Pécs, Pécs 7624, Hungary*
[2]*Szentágothai Research Centre, University of Pécs, Pécs, Hungary*
[3]*ELKH-PTE High-Field Terahertz Research Group, Pécs, Hungary*
[4]*Service OPERA-Photonique, Université Libre de Bruxelles (ULB), Brussels, Belgium*
[5]*tibai@fizika.ttk.pte.hu*
[6]*spencer.jolly@ulb.be*

Abstract: We present an improved model for electron acceleration in vacuum with high-energy THz pulses that includes spatiotemporal effects. In our calculations, we examined the acceleration with 300 GHz and 3.0 THz central frequency THz pulses with properties corresponding to common sources, and compared the Gaussian and Poisson spectral amplitudes and the associated time profiles of the electric fields. Our calculation takes into account both the longitudinal field and the spatio-spectral evolution around the focus. These aspects of the model are necessary due to the tight focusing and the duration towards a single-cycle of the THz pulses, respectively. The carrier-to-envelope phase (CEP) and the tilting angle of the coincident few- or single-cycle THz pulses must be tuned in all cases in order to optimize the acceleration scheme. We reveal additionally that electron beams with different final energies and different divergences can be generated based on simulated THz pulses having different Porras factors, describing the frequency dependence of the spatiotemporal amplitude profile, which may depend strongly on the method used to generate the single-cycle THz pulses.

1. Introduction

Terahertz (THz) science [1,2] has become an increasingly important realm of the optical sciences, allowing for novel metrology and inspection sources among other applications. However, the generation of coherent THz radiation has historically been difficult due to the availability and maturity of materials with advantageous properties in the THz range. Taking advantage of increasingly sophisticated technology [3], the production of THz pulses from nonlinear-optical sources has progressed such that energies approaching or exceeding 1 mJ are possible [4–13] for few- or single-cycle pulse that, when focused, produce fields well exceeding 10 MV/cm.

Acceleration and manipulation of electrons with high-field THz pulses has been investigated and demonstrated in structured dielectric devices using single-cycle THz pulses [14–18] and dielectric-lined waveguides using multi-cycle THz pulses [19–23]. These techniques have allowed both controlled acceleration of electrons by tens of keV, and also streaking, pulse compression, and staged combinations of each operation.

The direct acceleration of electrons to relativistic energies with high-field single-cycle THz pulses has been predicted via simulations [24]. This scenario is shown in Fig. 1 whereby two identical mostly counter-propagating THz pulses produce a net electric field in one direction, but their magnetic fields are canceled. If an electron is injected or born via ionization near the last zero-crossing of the field before the pulse peak, then the electron can be accelerated to mildly relativistic energies. Experimentally this electron injection is envisaged as localized ionization due to a femtosecond laser pulse at optical wavelengths, the same as the pump for the THz source, practically possible due to the long wavelength of the THz radiation (1 mm).

A complete multi-stage infrastructure for producing 8 fC electron bunches with up to 340 keV energy, only 2.0% energy spread and compressed on-target duration of 200 fs has been recently designed [25].
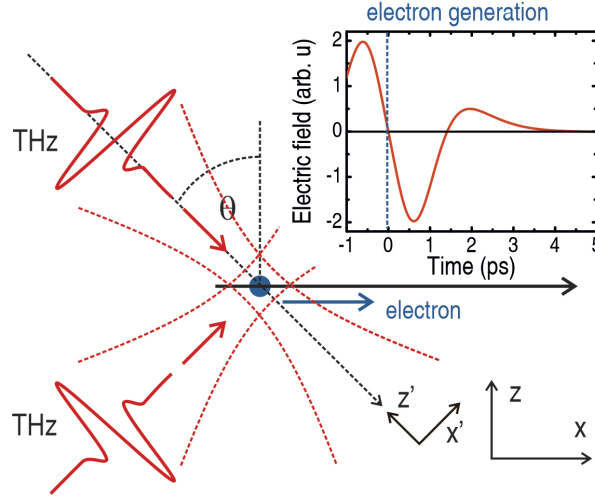

Fig. 1. The scenario under consideration in this work. Two identical THz-pulse are coincident at a focus with a certain carrier-to-envelope phase (CEP) and angle θ such that they produce a net longitudinal field and zero transverse electric field (counter-propagating when $\theta = 0$). The electron is assumed to be born when the field becomes accelerating (negative) as shown in the inset for a given CEP.

Still, the propagation and field evolution of few- or single-cycle THz pulses becomes non-trivial due to the chromatic nature of diffraction [26–28]. Additionally, the spectral shape must be modified such that the amplitudes of the negative frequencies are strictly zero [29] in order to correspond to a rigorous physical solution. Therefore the initial model must be modified. We present first results with the most simple modified model, and compare them to the case with a Gaussian spectral profile and without considering the chromatic nature of diffraction (i.e., with previously considered simplifications). Then we consider THz pulses having a varying frequency-dependent beam waist, which further complicates the results.

2. Details of the model

The field of a tightly-focused electromagnetic wave linearly-polarized (in the x'-direction) at frequency ω is

$$\vec{E}(x', z', \omega) = E_0 \frac{w_0}{w(z')} e^{-x'^2/w(z')^2} e^{i\psi}$$
$$\times \left[\hat{x}' - \frac{2ix'}{k} \left(\frac{1}{w(z')^2} + \frac{k}{2iR(z')} \right) \hat{z}' \right] \tag{1}$$

$$\psi(z') = kz' - \omega t + \frac{kx'^2}{2R(z')} - \eta(z') + \phi_0, \tag{2}$$

where $w(z') = w_0\sqrt{1 + (z'/z_R)^2}$ is the evolving beam radius, $R(z') = z'[1 + (z'/z_R)^2]$ is the radius of curvature, $\eta(z') = \arctan(z'/z_R)$ is the Gouy phase along the propagation direction (z'), and ϕ_0 is the carrier-to-envelope phase (CEP). The beam waist is w_0 with the Rayleigh range $z_R = \omega w_0^2/2c$ and $k = \omega/c$. The consideration of the vector nature around the focus at

$z = 0$—seen in the non-zero field along $\hat{z}'$—is necessary when the focused spot size w_0 becomes comparable with the wavelength $\lambda = 2\pi c/\omega$ [30,31].

When including the effect of the tilt angle θ the field in Eq. (1) has to be transformed according to $x' = x\cos(\theta) - z\sin(\theta)$ and $z' = x\sin(\theta) + z\cos(\theta)$, producing the field in the fixed coordinate system of the electron. When two identical pulses are coincident on the same focus, then symmetry enforces that the electric field is purely along the x-direction and the magnetic fields cancel such that, when z=0 for example,

$$\vec{E}(x,\omega) = 2E_0 \frac{w_0}{w(x\sin(\theta))} e^{-(x\cos(\theta))^2/w(x\sin(\theta))^2} e^{i\psi(x\sin(\theta))}$$
$$\times \left[\cos(\theta) - \sin(\theta)\frac{2ix\cos(\theta)}{k} \left(\frac{1}{w(x\sin(\theta))^2} + \frac{k}{2iR(x\sin(\theta))} \right) \right] \hat{x}. \tag{3}$$

To model a tightly-focused pulse with a pulse width approaching single-cycle, a spectral amplitude profile is needed that is wide enough to support the short duration but has zero DC and negative frequency components. A Poisson spectral amplitude

$$A(\omega) \propto \left(\frac{s\omega}{\omega_0} \right)^{s+1} \left(\frac{1}{\omega} \right) \frac{e^{-s\omega/\omega_0}}{\Gamma(s+1)}, \tag{4}$$

is a suitable choice to rigorously describe the spectral content of the pulse [29] and resembles that produced in common single-cycle THz sources. The central frequency is ω_0 and the spectral width increases with decreasing s corresponding to a shorter temporal duration. The need for this spectral weighting can be seen in Fig. 2(a) when the Poisson case is compared to the Gaussian case for $\omega_0 = 2\pi \times 300\,\text{GHz}$ and $s = 3.85$. The Gaussian profile has non-zero amplitude at zero (and negative) frequencies because the spectral width has approached the magnitude of the central frequency. It should be noted that as s becomes large ($s \gg 10$) the Poisson profile approaches the standard Gaussian, so this general description is useful.
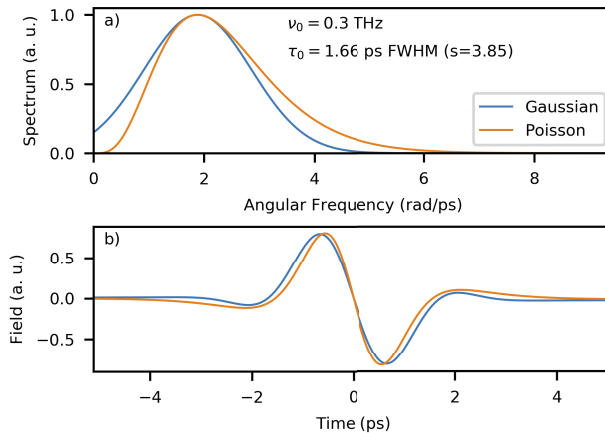

Fig. 2. Comparison of the Gaussian and Poisson spectral amplitude (a) and temporal field (b) for the 300 GHz case.

The Poisson spectral profile results in the following temporal profile $A(t) = FT[A(\omega)]$

$$A(t) \propto \left(\frac{is/\omega_0}{t + is/\omega_0} \right)^{s+1}, \tag{5}$$

visualized in Fig. 2(b) and compared to the case of a Gaussian with a similar duration. Note the significantly longer tails in the Poisson case, which correspond to the more physically correct

situation, where the temporal envelope changes shape as it approaches a single cycle. For example, the Poisson temporal profile at this duration no longer has the same relationship between FWHM and $1/e^2$ width as a Gaussian pulse.

Besides the different pulse shape at $z = r = 0$ due to the Poisson spectral amplitude, the propagation of a few- or single-cycle pulse is also more accurately described by considering the chromatic nature of diffraction [27]. Generally the beam can be represented in frequency space and Fourier-transformed to time. In our case this is achieved numerically by describing the fields using many frequency components which effectively make up the Fourier series of the temporal field

$$\vec{E}(r, z, t) \propto \sum_{\omega} \vec{E}(r, z, \omega) \times A(\omega) \times e^{i\omega t}, \tag{6}$$

that describes the field in real time as it propagates.

Finally, we use the electric field described above to simulate the interaction of two perfectly overlapped and coincident THz pulses on the electron (as sketched in Fig. 1). This electron acceleration is modelled using the relativistic Lorentz force equations in the General Particle Tracer (GPT) software [32]. The software allows for simulating particle trajectories, but also for the acceleration of electron beams including space-charge effects.

All of these ingredients: the inclusion of the longitudinal component of the tightly-focused field, the Poisson spectral profile, and the propagation using the Fourier components add a significantly enhanced rigour to the simulations of electron acceleration, which should increase confidence and accuracy in predicting and describing future experiments.

3. Results

As mentioned in the previous section, in this work we consider two possible THz pulses with cutting-edge or near-future levels of THz pulse energy at frequencies and pulse durations corresponding to the parameters of two different source materials. These parameters are summarized in Table 1.

Table 1. The physical scenarios considered in this work corresponding to 1 mJ of pulse energy.[a]

ν_0 (THz)	Δt (ps)	s	w_{00} (mm)	E_0 (MV/cm)
0.3	1.66	3.85	1.0	5.21
3.0	0.36	17	0.1	113

[a]The pulse duration is the FWHM and w_{00} is the beam waist at the central frequency.

The 300 GHz case corresponds to Lithium Niobate sources [13] and the 3 THz to organic crystal sources such as those using DAST or DSTMS [9]. One important difference is that we assume focusing to a beam waist of λ in both cases, which means that the 3 THz case is much more tightly focused and thereby the peak electric field is much higher. Although organic crystal sources have a mean frequency extending further to a few-THz, their relative bandwidth is smaller than in the case of Lithium Niobate, meaning that the 300 GHz case is closer to single-cycle ($s = 3.85$) than the 3 THz case ($s = 17$). These values for s are chosen specifically to match the FWHM pulse duration defined in Table 1.

Now that the model has been outlined, we can assess the results in these two cases with the new intricacies included. We hypothesize that the longitudinal field is important for both cases due to their tight focusing and therefore the inclusion of the non-paraxial addition in Eq. (1) is useful. However, because of the fact that the 300 GHz case is much closer to single-cycle, we guess that the spatiotemporal aspects will be much more important in that case.

First, for a CEP = 0 (a sine field in our case as in Fig. 2(b)) and the 300 GHz case, we compare the new model, i.e., a Poisson spectral envelope and chromatic diffraction, with a Gaussian and a non-developing temporal envelope (i.e., without considering spatiotemporal propagation). Both cases were numerically simulated with and without the longitudinal field included. The electric field experienced by an electron as it is accelerated is shown in Fig. 3(a) for CEP = 0 (sine) and $\theta = 0$ (counter-propagating pulses). The electron experiences a similar peak accelerating field in both cases, but in the Poisson case it experiences a greater integrated decelerating field resulting in a lower final energy. This simulation only includes the zero tilting angle case, so the difference in the final energy is caused only by the pulse shape, due to the longer tails of the Poisson case that can be seen in Fig. 2.
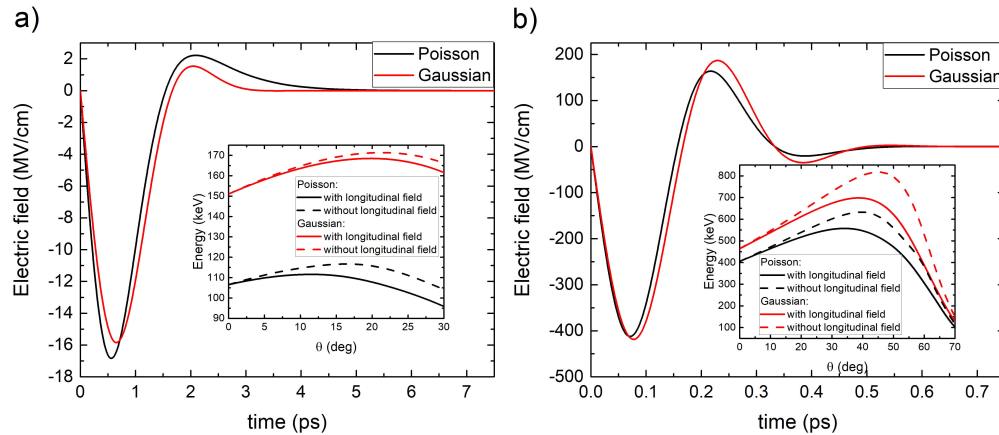

Fig. 3. Comparison of electron acceleration with CEP = 0 (sine) for the 300 GHz (a) and 3 THz (b) high-field ($2 \times E_0$) cases with a Gaussian spectral envelope and a no spatiotemporal evolution (Gaussian, red lines) and a Poisson spectral envelope and full spectral propagation (Poisson, black lines). The perceived field is shown with $\theta = 0$ for the case of Gaussian and Poisson including the longitudinal field. The final electron energy is shown with (solid) and without (dashed) inclusion of the longitudinal field (inset) as a function of θ.

In case of the Gaussian spectral profile the final electron energy is smaller with ∼28% compared to the Poisson case at $\theta = 0$. On the other hand, there is not a significant additional difference between the results from the Gaussian and Poisson spectral profiles when θ is increased above zero, seen in the inset of Fig. 3(a). In both cases there is a slight decrease in the electron energy when adding the longitudinal field correction, more pronounced in the Poisson case. This is sensible since at $\theta = 0$ the longitudinal component should have no impact according to Eq. (3). Note that in Eq. (1) the longitudinal field is out of phase with the transverse field, hence the slight decrease once the longitudinal field has an impact. The 3 THz case is shown in Fig. 3(b) with qualitatively similar results, although the multi-cycle nature of the field means that the difference Gaussian-Poisson is smaller, and the change is greater when increasing θ due to the higher peak field.

Considering the Poisson spectrum along with full propagation of the different spectral components and taking into account the longitudinal field component, the optimization with both the angle θ and the CEP can be performed for varying levels of the peak electric field. We suppose that these corrections become more important at higher accelerating fields, which can be motivated by the fact that the $\hat{z}'$ component in Eq. (1) is only non-zero at off-axis positions ($x' \neq 0$). As the electron is accelerated further by larger accelerating fields, it travels to farther positions off-axis while the THz pulse is still present, thus traversing a larger portion of the focal volume.

The map of the final electron energy as a function of CEP and θ can be seen for the lowest and highest field levels simulated in the upper panels of Fig. 4, for both the 300 GHz (a–b) and 3 THz cases (c–d). The results of the optimization at many power levels is shown in Figs. 4(e)–(f), with the optimum CEP and θ is shown in black where the optimum final electron energy is shown in blue. Sensibly, the optimum energy increases roughly with the square of the peak field, and for every case the optimum θ also increases monotonically with the increasing peak electric field (the optimum θ is larger in the case of 3 THz due mostly to the higher absolute electric field). This result is in accordance with past work [24,25] where in the case of a higher field and $\theta = 0$ the accelerated electron leaves the THz field sooner, but by increasing the value of θ the electron will overlap with the accelerating field for longer resulting in a higher final energy. Notably, although the optimum CEP increases monotonically in the 300 GHz case, that is not so for 3 THz. This is likely due to the fact that the 3 THz pulses are not purely single-cycle and therefore they have a more complex acceleration trajectory.
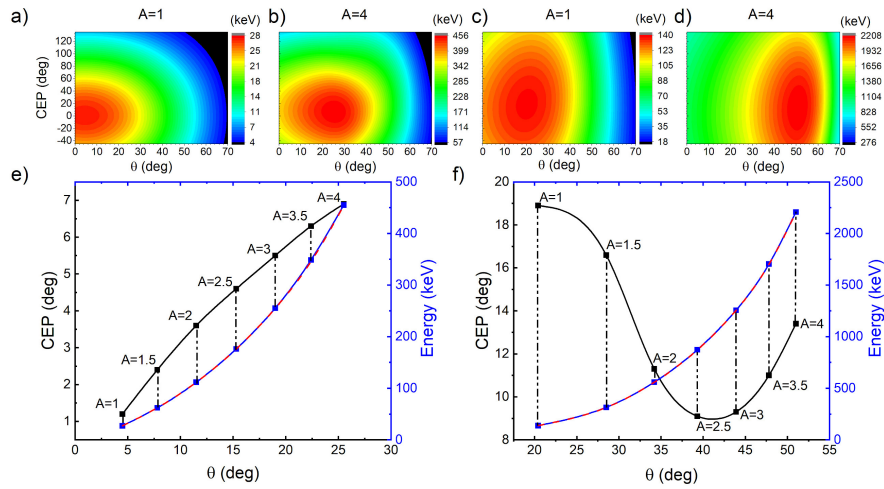

Fig. 4. Results of full optimization of both the CEP and the angle θ to achieve the highest electron energy for the 300 GHz case (left) and 3 THz (right) with different electric field levels ($E = A \times E_0$). The lowest field ($1 \times E_0$) and highest field ($4 \times E_0$) are shown in the top-left and top-right panels respectively for each case (300 GHz (a)–(b) and 3 THz cases (c)–(d)). The optimum CEP and θ values of the driving THz pulses (black) and the final electron energies (blue) are shown for several values of the peak field for 300 GHz (e) and 3 THz (f). The final energies at CEP = 0 are shown with the dashed red lines, essentially agreeing with those at the optimum CEP.

4. Larger set of spatiotemporal amplitudes

Beside the case presented in the previous section where all frequencies have the same beam waist, but are then all propagated separately, the frequency-dependence of the beam waist can be more arbitrary [33,34]. Such beam waist variations with frequency have been measured in high-power lasers [35] and are an intrinsic property of broadband THz sources based on different technologies [36,37]. This can be represented by the "Porras factor" g_0, which is calculated in the following way

$$g_0 = - \left. \frac{dz_R}{d\omega} \right|_{\omega_0} \frac{\omega_0}{z_R(\omega_0)}, \tag{7}$$

where z_R is the Rayleigh range in the focus. Essentially, g_0 describes the linear coefficient in the Taylor expansion of the Rayleigh range on a beam before focusing, which is therefore the negative

of the coefficient in the Taylor expansion of the Rayleigh range on a beam in the focus. The case of the previous section was implicitly at $g_0 = -1$ because the chromatic nature of diffraction was included, but the beam waist in-focus was assumed to be independent of the frequency. The definition of g_0 means that in the most general case the beam waist depends on frequency as $w_0(\omega) = w_{00} (\omega_0/\omega)^{(g_0+1)/2}$, where w_{00} is the waist at the central frequency.

The transverse fields for the three values of g_0 that we will consider, -1, 0, and +1, are shown in Fig. 5 at $z = 0$. With $g_0 = -1$, a constant beam waist as in the previous section, the fields do not vary with space and will only develop spatiotemporal variation as the beam propagates away from $z = 0$. For the two other cases, $g_0 = 0$ and +1, there is a clear spatial dependence of the pulse duration and implicitly its shape as well. The fields on the axis ($x = 0$) are compared to each other in Fig. 5 (bottom), where the variation of the peak electric field based on the Porras factor can be clearly seen. We consider the cases of -1, 0, and +1 as examples, since there is only a small amount of experimental work characterizing THz sources spatiotemporally, and the expected Porras factor would likely depend on many experimental parameters.
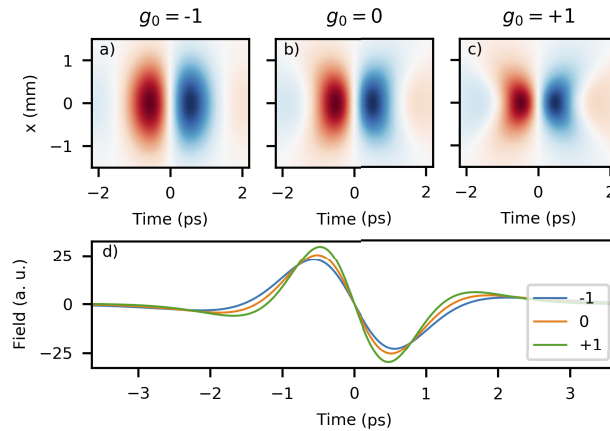

Fig. 5. spatio-temporal transverse fields directly in the focus for the 300 GHz case for $g_0 = $ -1, 0, +1 (top) with the on-axis fields compared (bottom).

The results of the electron acceleration via pulses with these various g_0 values, for both the 300 GHz and 3 THz cases with parameters indicated in Table 1, and for four different levels of electric field strength are shown in Fig. 6. The results are presented as a function of θ at the optimum CEP for each specific case. For both 300 GHz and 3 THz the improvement when increasing θ becomes larger when increasing the peak electric field.

For both the 300 GHz and 3 THz case $g_0 = -1$ provides the optimum acceleration when $\theta = 0$, despite having a lower peak field in the focus (see Fig. 5) but when θ is increased $g_0 = +1$ becomes more optimal. It is important to note that the optimum θ is not the same for each g_0 value, nor is the optimum CEP (not shown), and that the difference for different g_0 values becomes more significant as the peak field is increased. In general, the differences just explained for the different g_0 values are larger for the 300 GHz case owing to it's relatively shorter duration ($s = 3.85$) compared to the 3 THz case ($s = 17$). With this relatively shorter duration the spatiotemporal effects become more important.

Our analysis so far has only concerned the final electron energies, but especially in this case of varying g_0 parameter there can be effects on the properties of a bunch of electrons with finite charge and spatial extent. Figure 7 shows the divergence of the electron bunch for both the 300 GHz and 3 THz cases in the case of a simulated bunch of 20 fC and size of 5 μm (rms.) [24]. The difference in divergence between the different g_0 cases is significantly more pronounced in the 300 GHz case, again most likely due to its much shorter relative duration. This shows
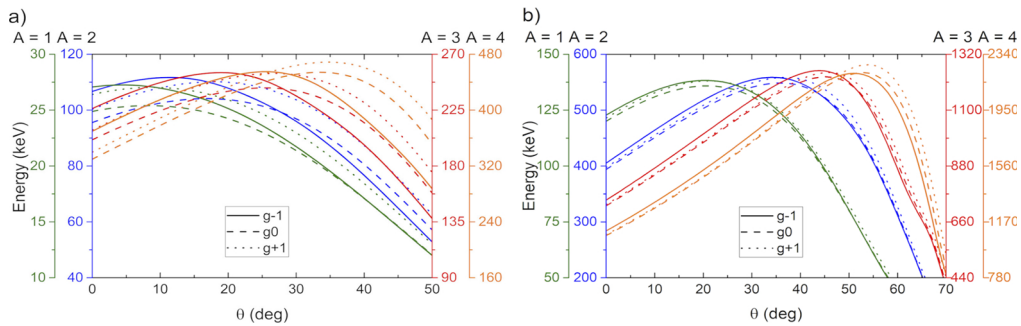
Fig. 6. Final electron energy for the 300 GHz (left) and 3 THz (right) cases for $g_0 = -1$, 0, +1 (solid, dashed, dotted) for the four levels of electric field strength (green, blue, red, orange—$E = A \times E_0$) as a function of θ at the optimum CEP for each case.

that, beyond effecting the final energy or the optimum CEP and θ, the spatio-spectral amplitude variation encompassed by g_0 has important effects on an electron beam, which is extremely relevant for applications and staging of such acceleration.
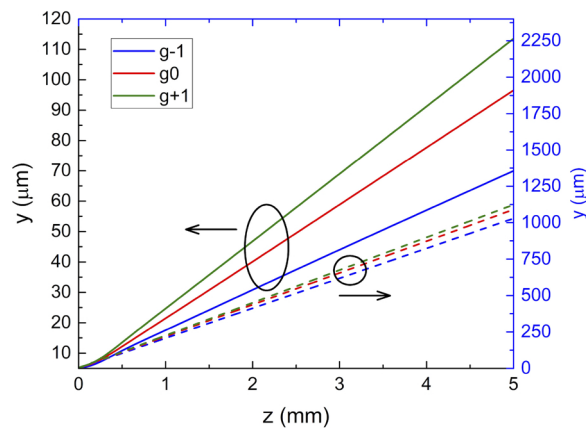

Fig. 7. Divergence in the y-z plane for the 300 GHz (solid, left axis) and 3 THz (dashed, right axis) high-field ($2 \times E_0$) case for $g_0 = -1$, 0, +1 (blue, red, green) when accelerating an electron bunch with an initial size of 5 μm.

5. Conclusion

We have presented a refined and more accurate model for direct acceleration of electrons using coincident, mostly counter-propagating, tightly-focused ultrashort THz pulses. The model included the modeling of the longitudinal field necessary due to the tight focusing, the Poisson spectral amplitude shape due to the duration towards a single-cycle, and the propagation of the pulse taking into account the chromatic nature of propagation—also significant due to the single-cycle duration of the pulses.

Although these results were specific to the case of counter-propagating THz pulses in a vacuum, similar effects would be more important as the field strength of the accelerating pulses increases or the beam waist decreases, since the accelerated electrons would traverse a larger portion of the focal volume. For this reason, the modeling is important more broadly for the acceleration and dynamics of free-electrons under the influence of few- or single-cycle electromagnetic fields, even

at much higher frequencies than the THz range. Other THz-based accelerations schemes such as acceleration in waveguide structures could be similarly affected by the Poisson distribution and Porras factor, although this would only be the case when the pulse remains close to single-cycle and the waveguide allows for multi-mode coupling.

Practically for the scenario considered, the most important conclusion is that for optimization of the electron energy both the CEP and propagation angle θ must be tuned, and that depending on the spatiospectral amplitude profile the divergence will be asymmetric. Knowledge of the spatiotemporal or spatiospectral field of the THz source in use for acceleration, which can become non-trivial depending on the method of pulse generation [36–38], allows for predicting the performance of such an electron accelerator and for better comparison to numerical predictions. Furthermore, more complex spatiotemporal fields may provide for optimization of the THz-based acceleration process as has been shown in various other laser-based acceleration scenarios [39–42].

Disclosures. The authors declare no conflicts of interest.

Data availability. Data underlying the results presented in this paper are not publicly available at this time but may be obtained from the authors upon reasonable request.

References

1. J. Hebling, K. L. Yeh, M. C. Hoffmann, and K. A. Nelson, "High-power THz generation, THz nonlinear optics, and THz nonlinear spectroscopy," IEEE J. Sel. Top. Quantum Electron. **14**(2), 345–353 (2008).
2. T. Kampfrath, K. Tanaka, and K. A. Nelson, "Resonant and nonresonant control over matter and light by intense terahertz transients," Nat. Photonics **7**(9), 680–690 (2013).
3. P. Salén, M. Basini, S. Bonetti, J. Hebling, M. Krasilnikov, A. Y. Nikitin, G. Shamuilov, Z. Tibai, V. Zhaunerchyk, and V. Goryashko, "Matter manipulation with extreme terahertz light: Progress in the enabling thz technology," Phys. Rep. **836-837**, 1–74 (2019).
4. J. A. Fülöp, L. Pálfalvi, G. Almási, and J. Hebling, "Design of high-energy terahertz sources based on optical rectification," Opt. Express **18**(12), 12311–12327 (2010).
5. J. A. Fülöp, L. Pálfalvi, M. C. Hoffmann, and J. Hebling, "Towards generation of mJ-level ultrashort THz pulses by optical rectification," Opt. Express **19**(16), 15090–15097 (2011).
6. J. A. Fülöp, L. Pálfalvi, S. Klingebiel, G. Almasi, F. Krausz, S. Karsch, and J. Hebling, "Generation of sub-mJ terahertz pulses by optical rectification," Opt. Lett. **37**(4), 557–559 (2012).
7. J. A. Fülöp, Z. Ollmann, C. Lombosi, C. Skrobol, S. Klingebiel, L. Pálfalvi, F. Krausz, S. Karsch, and J. Hebling, "Efficient generation of THz pulses with 0.4 mJ energy," Opt. Express **22**(17), 20155–20163 (2014).
8. C. Vicario, B. Monoszlai, and C. P. Hauri, "GV/m single-cycle terahertz fields from a laser-driven large-size partitioned organic crystal," Phys. Rev. Lett. **112**(21), 213901 (2014).
9. C. Vicario, A. V. Ovchinnikov, S. I. Ashitkov, M. B. Agranat, V. E. Fortov, and C. P. Hauri, "Generation of 0.9-mJ THz pulses in DSTMS pumped by a $Cr:Mg_2SiO_4$ laser," Opt. Lett. **39**(23), 6632–6635 (2014).
10. G. Tóth, L. Pálfalvi, Z. Tibai, L. Tokodi, J. A. Fülöp, Z. Márton, G. Almási, and J. Hebling, "Single-cycle scalable terahertz pulse source in reflection geometry," Opt. Express **27**(21), 30681–30691 (2019).
11. G. o Krizsán, Z. Tibai, J. Hebling, L. Pálfalvi, G. Almási, and G. Tóth, "Lithium niobate and lithium tantalate based scalable terahertz pulse sources in reflection geometry," Opt. Express **28**(23), 34320–34327 (2020).
12. G. Tóth, L. Pálfalvi, S. Turnár, Z. Tibai, G. Almási, and J. Hebling, "Performance comparison of lithium-niobate-based extremely high-field single-cycle terahertz sources [invited]," Chin. Opt. Lett. **19**(11), 111902 (2021).
13. B. Zhang, Z. Ma, J. Ma, X. Wu, C. Ouyang, D. Kong, T. Hong, X. Wang, P. Yang, L. Chen, Y. Li, and J. Zhang, "1.4-mJ high energy terahertz radiation from lithium niobates," Laser Photonics Rev. **15**(3), 2000295 (2021).
14. A. Fallahi, M. Fakhari, A. Yahaghi, M. Arrieta, and F. X. Kärtner, "Short electron bunch generation using single-cycle ultrafast electron guns," Phys. Rev. Accel. Beams **19**(8), 081302 (2016).
15. W. R. Huang, A. Fallahi, X. Wu, H. Cankaya, A.-L. Calendron, K. Ravi, D. Zhang, E. A. Nanni, K.-H. Hong, and F. X. Kärtner, "Terahertz-driven, all-optical electron gun," Optica **3**(11), 1209–1212 (2016).
16. D. Zhang, A. Fallahi, M. Hemmer, X. Wu, M. Fakhari, Y. Hua, H. Cankaya, A.-L. Calendron, L. E. Zapata, N. H. Matlis, and F. X. Kärtner, "Segmented terahertz electron accelerator and manipulator (STEAM)," Nat. Photonics **12**(6), 336–342 (2018).

17. A. Fallahi and F. X. Kärtner, "Design strategies for single-cycle ultrafast electron guns," J. Phys. B: At., Mol. Opt. Phys. **51**(14), 144001 (2018).

18. D. Zhang, A. Fallahi, M. Hemmer, H. Ye, M. Fakhari, Y. Hua, H. Cankaya, A.-L. Calendron, L. E. Zapata, N. H. Matlis, and F. X. Kärtner, "Femtosecond phase control in high-field terahertz-driven ultrafast electron sources," Optica **6**(7), 872–877 (2019).

19. L. J. Wong, A. Fallahi, and F. X. Kärtner, "Compact electron acceleration and bunch compression in THz waveguides," Opt. Express **21**(8), 9792–9806 (2013).

20. E. A. Nanni, W. R. Huang, K.-H. Hong, K. Ravi, A. Fallahi, G. Moriena, R. J. D. Miller, and F. X. Kärtner, "Terahertz-driven linear electron acceleration," Nat. Commun. **6**(1), 8486 (2015).

21. F. Lemery, K. Flöttmann, P. Piot, F. X. Kärtner, and R. W. Assman, "Synchronous acceleration with tapered dielectric-lined waveguides," Phys. Rev. Accel. Beams **21**(5), 051302 (2018).

22. D. Zhang, M. Fakhari, H. Cankaya, A.-L. Calendron, N. H. Matlis, and F. X. Kärtner, "Cascaded multicycle terahertz-driven ultrafast electron acceleration and manipulation," Phys. Rev. X **10**(1), 011067 (2020).

23. M. T. Hibberd, A. L. Healy, D. S. Lake, V. Georgiadis, E. J. H. Smith, O. J. Finlay, T. H. Pacey, J. K. Jones, Y. Saveliev, D. A. Walsh, E. W. Snedden, R. B. Appleby, G. Burt, D. M. Graham, and S. P. Jamison, "Acceleration of relativistic beams using laser-generated terahertz pulses," Nat. Photonics **14**(12), 755–759 (2020).

24. Z. Tibai, M. Unferdorben, S. Turnár, A. Sharma, J. A. Fülöp, G. Almási, and J. Hebling, "Relativistic electron acceleration by focused thz pulses," J. Phys. B: At., Mol. Opt. Phys. **51**(13), 134004 (2018).

25. S. Turnár, J. Hebling, J. A. Fülöp, G. Tóth, G. Almási, and Z. Tibai, "Design of a thz–driven compact relativistic electron source," Appl. Phys. B **127**(3), 38 (2021).

26. M. A. Porras, "Ultrashort pulsed gaussian light beams," Phys. Rev. E **58**(1), 1086–1093 (1998).

27. M. A. Porras, "Nonsinusoidal few-cycle pulsed light beams in free space," J. Opt. Soc. Am. B **16**(9), 1468–1474 (1999).

28. M. A. Porras, "Diffraction effects in few-cycle optical pulses," Phys. Rev. E **65**(2), 026606 (2002).

29. C. F. R. Caron and R. M. Potvliege, "Free-space propagation of ultrashort pulses: Space-time couplings in gaussian pulse beams," J. Mod. Opt. **46**(13), 1881–1891 (1999).

30. L. W. Davis, "Theory of electromagnetic beams," Phys. Rev. A **19**(3), 1177–1179 (1979).

31. J. P. Barton and D. R. Alexander, "Fifth-order corrected electromagnetic field components for a fundamental gaussian beam," Appl. Phys. Lett. **66**, 2800–2802 (1989).

32. "Pulsar Physics and the General Particle Tracer (GPT) code," http://www.pulsar.nl/gpt/.

33. M. A. Porras, "Characterization of the electric field of focused pulsed gaussian beams for phase-sensitive interactions with matter," Opt. Lett. **34**(10), 1546–1548 (2009).

34. M. A. Porras, Z. L. Horváth, and B. Major, "Three-dimensional carrier-envelope-phase map of focused few-cycle pulsed gaussian beams," Phys. Rev. A **98**(6), 063819 (2018).

35. D. Hoff, M. Krüger, L. Maisenbacher, A. M. Sayler, G. G. Paulus, and P. Hommelhoff, "Tracing the phase of focused broadband laser pulses," Nat. Phys. **13**(10), 947–951 (2017).

36. M. T. Hibberd, D. S. Lake, N. A. B. Johansson, T. Thompson, S. P. Jamison, and D. M. Graham, "Magnetic-field tailoring of the terahertz polarization emitted from a spintronic source," Appl. Phys. Lett. **114**(3), 031101 (2019).

37. G. A. Hine and M. Doleans, "Intrinsic spatial chirp of subcycle terahertz pulsed beams," Phys. Rev. A **104**(3), 032229 (2021).

38. L. Wang, G. Tóth, J. Hebling, and F. X. Kärtner, "Tilted-pulse-front schemes for terahertz generation," Laser Photonics Rev. **14**(7), 2000021 (2020).

39. S. W. Jolly, "Influence of longitudinal chromatism on vacuum acceleration by intense radially polarized laser beams," Opt. Lett. **44**(7), 1833–1836 (2019).

40. C. Caizergues, S. Smartsev, V. Malka, and C. Thaury, "Phase-locked laser-wakefield electron acceleration," Nat. Photonics **14**(8), 475–479 (2020).

41. S. W. Jolly, "On the importance of frequency-dependent beam parameters for vacuum acceleration with few-cycle radially-polarized laser beams," Opt. Lett. **45**(14), 3865–3868 (2020).

42. L. Wang, U. Niedermayer, J. Ma, W. Liu, D. Zhang, and L. Qian, "Spatio-temporal coupling controlled laser for electron acceleration," arXiv:2201.12758 (2022).